Chapter 2
Thin Amorphous Fe–Tb Alloy Films

Until the mid 20th century the spontaneous magnetization was believed to require long range order, which is only given in crystalline materials. Interestingly, in 1946 H. König [1] found ferromagnetism in thin Fe films, which were deposited on cooled substrates. Although electron diffraction measurements revealed an amorphous structure the ferromagnetic behavior was traced to small crystallites embedded in the film. Since 1970 the existence of amorphous magnetic materials is proofed and commonly accepted by the physical community. By today comprehensive knowledge about the origin of amorphous magnetism exists. Many different systems are discussed in the literature [2–5]. On this account the present chapter focuses on the discussion of thin amorphous Fe–Tb alloy films as particular system important concerning this work.

2.1 Phase Diagram

The binary rare-earth-transition-metal alloy system consisting of terbium and iron exhibits four stable crystalline phases $Fe_{17}Tb_2$, $Fe_{23}Tb_6$, Fe_3Tb, and Fe_2Tb as outlined in the phase diagram in Fig. 2.1 for bulk samples in thermal equilibrium [6–8]. The ferromagnetic (F) $Fe_{17}Tb_2$ and $Fe_{23}Tb_6$ phases coexist in the composition range from 10.5 to 20.7 at.% Tb together with α-Fe. For a Tb content higher than 20.7 at.% and smaller than 25 at.% mixed phases arise consisting of α-Fe and ferrimagnetic (FI) Fe_3Tb clusters. Higher portions of Tb produce mixed phases of α-Fe and FI Fe_2Tb up to compositions around 33 at.% Tb. Outside the described composition range a mixture of α-Fe and α-Tb clusters exist. The crystal structure, Curie temperature, and magnetic configuration of all four crystalline phases are listed in Table 2.1 [9].

The formation of stable crystalline phases in the composition range from 10.5 at.% to around 33 at.% Tb occurs only for bulk material coming from the liquid phase. Thin films behave different. Using magnetron co-sputtering, a common technique to produce thin metallic alloy films, deposited Fe–Tb layers reveal an amorphous structure [10–12]. At room temperature (RT) the amorphous structure is stable, since the

C. Schubert, *Magnetic Order and Coupling Phenomena*, Springer Theses,
DOI: 10.1007/978-3-319-07106-0_2, © Springer International Publishing Switzerland 2014

Table 2.1 Structural and magnetic properties of crystalline phases in the Fe–Tb alloy system [9]

Compound	Symmetry	Structure	Curie temperature (K)	Magnetic structure
$Fe_{17}Tb_2$	Hexagonal	$Ni_{17}Th_2$	408	F
$Fe_{23}Tb_6$	Cubic	$Mn_{23}Th_6$	574	F
Fe_3Tb	Rhombohedral	Ni_3Pu	648–655	FI
Fe_2Tb	Cubic	Cu_2Mg	696–711	FI

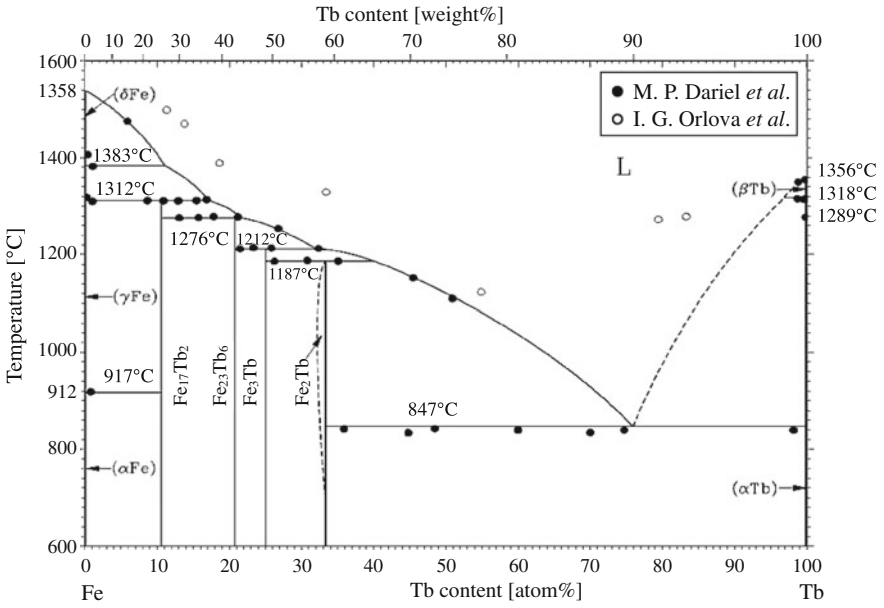

Fig. 2.1 Binary phase diagram of the $Fe_{100-x}Tb_x$ alloy system based on data from T. B. Massalski et al. [6] supplemented by several data points from M. P. Dariel et al. [7] and I. G. Orlova et al. [8] obtained from bulk samples in thermal equilibrium

crystallization in this system takes place not below 200 °C as it was found by N. Sato [13] for 1 µm thick Fe–Tb films. An overview about the composition dependence of the crystallization temperature is shown in Fig. 2.2. The temperature required for crystallization increases monotonous towards higher Tb contents. Although the literature provides no detailed discussion onto this, the enhancement of the crystallization temperature can be most likely attributed to the different phase mixtures present in this composition region.

Concerning the purpose of this work, the thin amorphous Fe–Tb alloy films were not exposed to temperatures higher than 450 K. Therefore, crystallization will be excluded in following annotations and discussions.

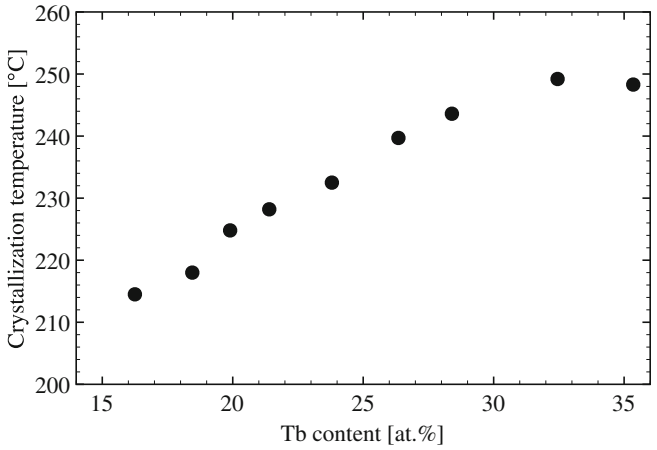

Fig. 2.2 Crystallization temperature of 1-μm-thick amorphous Fe–Tb alloy films as a function of the composition [13]

2.2 Intrinsic Magnetic Structure: Magnetic Anisotropy, Exchange Coupling, and Sperimagnetism

The common structures in magnetic materials, whether F, FI or antiferromagnetic (AF), are related to long range order and thus to crystalline structures. Although amorphous materials possess structural disorder collective magnetism exists. The chemical and structural disorder in this materials lead to a distribution in magnetic moment and exchange interaction. Furthermore, the varying interatomic distances induce random electrostatic fields giving rise to locally varying single ion anisotropy. In this manner the magnetic structure arises from the competition between exchange interaction trying to align magnetic moments and the local anisotropies due to the local structural order [3, 4, 14–16]. This can be described by the following model Hamiltonian for two subnetwork systems in particular valid for rare-earth-transition-metal alloys: [15, 17]

$$\mathcal{H} = -\sum \underline{D}_{\mathrm{a}} S_{\mathrm{a,z}}^2 - \sum \underline{D}_{\mathrm{b}} S_{\mathrm{b,z}}^2 - \sum J_{\mathrm{aa'}} \underline{S}_{\mathrm{a}} \cdot \underline{S}_{\mathrm{a'}} - \sum J_{\mathrm{ab}} \underline{S}_{\mathrm{a}} \cdot \underline{S}_{\mathrm{b}} - \sum J_{\mathrm{bb'}} \underline{S}_{\mathrm{b}} \cdot \underline{S}_{\mathrm{b'}}, \quad (2.1)$$

where a and b refer to different sites on the rare-earth and transition-metal subnetworks, respectively, $\underline{D}_{\mathrm{a,b}}$ denotes the distribution of local anisotropy, $\underline{S}_{\mathrm{a,b}}$ the spin, and $J_{\mathrm{aa'},\ldots}$ the exchange constant. Please note, z as index denotes the z-component of the spin. Normally the contributions $\underline{D}_{\mathrm{b}}$ and $J_{\mathrm{aa'}}$ are negligible. Depending on the values for the exchange and the local anisotropy asperomagnetic, speromagnetic and sperimagnetic configurations are possibles as outlined in Fig. 2.3.

In case of the Fe–Tb alloy system a sperimagnetic configuration arises. The magnetic exchange between the Fe and Tb moments occurs via 3d − 5d − 4f hybridization

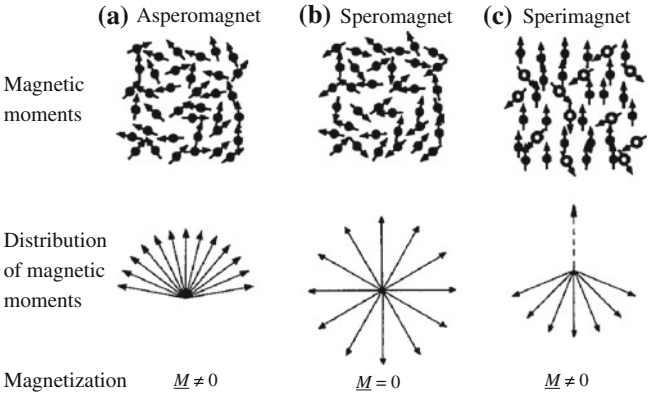

Fig. 2.3 Different magnetic configurations in amorphous one and two component systems. **a** Asperomagnet possessing a non-zero magnetization with a moment distribution pointing in a preferential direction. **b** Speromagnet exhibiting a zero magnetization due to a isotropic moment distribution. **c** Two subnetwork system with antiparallel moment distribution named sperimagnet [15]

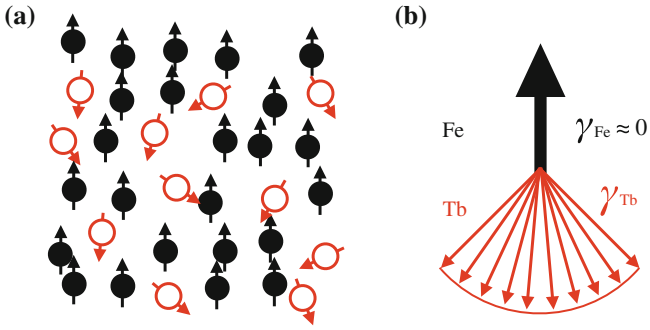

Fig. 2.4 **a** Moment distribution in a sperimagnetic material with antiparallel oriented magnetic sublattices. **b** Average magnetic moment distribution with angle γ in the amorphous Fe–Tb alloy system [15]

leading to an antiparallel alignment $J_{FeTb} < 0$ as known for heavy rare-earth-transition-metal alloys following Hund's rules [18]. Due to a strong interatomic Fe coupling $J_{FeFe'} > 0$ and a vanishing local anisotropy $\underline{D}_{Fe}$ for the iron sites a more or less collinear orientation of the Fe moments is observed. In contrast to this the Tb moments exhibit a weak exchange coupling $J_{TbTb'} << J_{FeFe'}$ and a strong distribution of the local anisotropy $\underline{D}_{Tb}$ producing a broad orientational distribution of the Tb moments as illustrated in Fig. 2.4. This moment distribution is commonly designated as fanning cone.

In thin amorphous Fe–Tb alloy films the growth conditions imprint a perpendicular magnetic anisotropy (PMA) meaning the resulting component of the fanning cone with respect to the Fe sublattice points perpendicular to the substrate plane.

The growth process induces an anisotropy in the short range order as observed by different groups [19–22]. This leads to different next neighbor distances and coordination numbers for Fe–Fe, Fe–Tb, and Tb–Tb pairs in out-of-plane and in-plane direction. In particular, a preference for unlike (i.e. Fe–Tb) near-neighbor pairs to align in out-of-plane direction was found. Due to this chemical anisotropy, the interaction of the local crystal field with the elongated shape of the 4f orbitals via spin-orbit coupling produces a magnetic anisotropy with an easy axis pointing along the out-of-plane direction. Often this is also described as single ion anisotropy of the Tb sites with preferential out-of-plane direction due to the exchange interaction among them and the Fe sublattice. Beside this origin of PMA magnetostriction [23] is known and will be discussed later.

2.3 Magnetic Properties with Regard to Alloy Composition, Film Thickness, and Temperature

Due to its sperimagnetic nature amorphous Fe–Tb alloy films possess manifold magnetic properties with particular temperature and composition dependencies. The present chapter is dedicated to give an overview of the different dependencies mainly focusing on saturation magnetization, coercivity, and magnetic anisotropy.

As previously mentioned heavy rare-earth-transition-metal alloys possess an antiparallel moment structure due to the parallel coupling of the orbital and spin moment in the rare-earth leading to an overall ferrimagnetic behavior. In consequence of the high magnetic moment of rare-earth metal ions (e.g., 9 μ_B per Tb ion) Fe–Tb alloy films are very sensitive to the amount of Tb they contain. Figure 2.5 shows the net saturation magnetization at RT, Curie temperature, and compensation temperature in (a) and the RT coercivity in (b) as a function of the Tb content of the alloy [11]. With increasing amount of Tb in the alloy the net saturation magnetization, which is dominated by the Fe sublattice decreases to zero towards the compensation composition at which the magnetic sublattices of Fe and Tb compensate each other. Above the compensation point the magnetization increases again towards higher Tb contents, while the dominant magnetic sublattice has changed from Fe to Tb. At room temperature the compensation composition is around 23 at.% [11]. Please note, the RT compensation composition can vary with different preparation techniques, since the compensation of the sublattice magnetic moments is strongly related to the intrinsic structure of the amorphous sperimagnetic alloy film. In particular the anisotropy in the chemical short range order and the shape of the fanning cone play an important role as discussed in the previous chapter.

Beside the compensation point at RT for 23 at.% Tb, other compensation temperatures (T_{Comp}) in the range up to the Curie temperature (T_C) of about 400 K are possible. Between 20 and 24 at.% Tb a compensation point exists (see Fig. 2.5a). For lower and higher amounts of Tb the Fe–Tb alloy films reveal a net magnetization

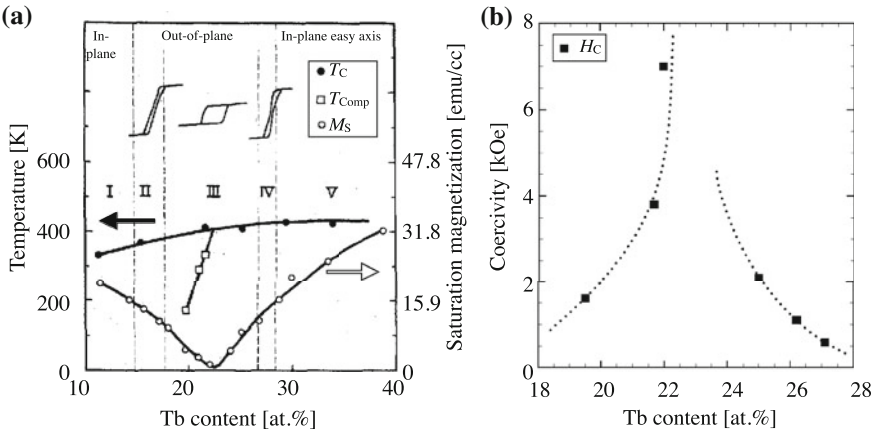

Fig. 2.5 **a** Curie temperature, compensation temperature, saturation magnetization, and **b** coercivity of amorphous Fe–Tb films with varying Tb concentration and a thickness of about 150 nm [11]. Please note that the magnetization and coercivity *curves* were obtained at room temperature. The *solid* and *dashed lines* serve as a guide to the eye. Region I and V correspond to the composition of Fe–Tb films with in-plane magnetic anisotropy. For compositions dedicated to region II, III, and IV the alloy films exhibit out-of-plane anisotropy, while the partition into the three regions takes the different shaped hysteresis loops into account. The increasing coercivity in (**b**) is caused by the RT compensation composition of about 23 at.%

dominated solely by the Fe and Tb sublattice, respectively, over the whole temperature range and no compensation point exists.

Concerning the Curie temperature only a slight dependency with regard to the alloy composition was observed. It decreases from about 400 to 350 K towards smaller amounts of Tb as presented in Fig. 2.5a. In comparison to pure crystalline Fe with $T_C \approx 1043$ K the values for amorphous Fe–Tb alloy films are significant smaller accounting for the weak exchange coupling between the Fe and Tb moments due to the 3d − 5d − 4f hybridization. The reason for the decrease in T_C towards smaller Tb contents lies in the reduction of the Fe–Fe next neighbor distances due to the less amount of larger Tb atoms in the alloy and the negative contribution of the Fe–Fe coupling term to T_C, as discussed in the literature [12]. Below 10 at.% Tb more and more crystalline bcc Fe grains exist leading to a strong increase in T_C towards the pure Fe value, when the Tb concentration becomes zero (not shown). A similar composition dependency as for the Curie temperature is also observed for the exchange stiffness A in the Fe–Tb alloy films as presented in Fig. 2.6a, since both values are related to each other.

Contrary to the net saturation magnetization the coercivity increases progressively in the vicinity of the compensation composition due to the inverse relation to the magnetization:

$$H_C \approx \frac{K_{\text{eff}}}{M_S}, \tag{2.2}$$

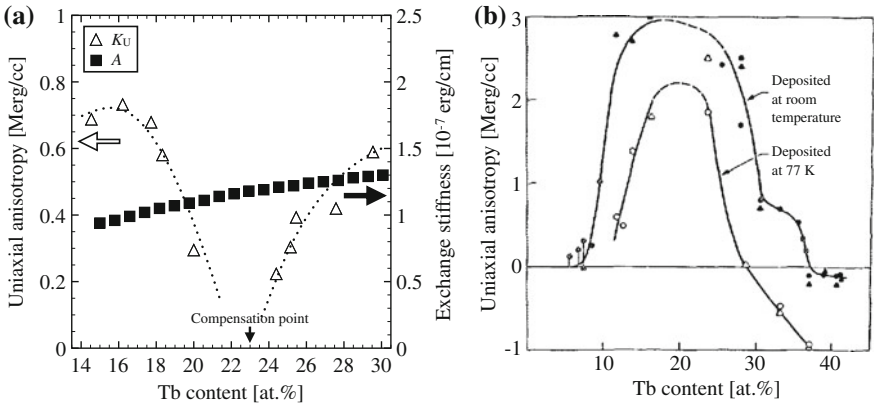

Fig. 2.6 **a** Uniaxial magnetic anisotropy K_U and calculated exchange stiffness A of 0.7 to 1.2 μm thick amorphous Fe–Tb alloy films at 298 K drawn as a function of the Tb content [24]. Details about the calculated data points are given in the text. **b** Uniaxial anisotropy of 500-nm-thick Fe–Tb films depending on the Tb content [25]. *Solid symbols* represent films deposited at room temperature, while open symbols denote films deposited on a liquid-nitrogen-cooled substrate. The *dashed* and *solid lines* serve as a guide to the eye

where H_C, K_{eff}, and M_S denote the coercivity, effective magnetic anisotropy, and net saturation magnetization, respectively. With regard to the anisotropy the given relation provides a useful lower estimation, which is exact within a factor of about 1 for amorphous ferrimagnetic rare-earth-transition-metal alloy films [3].

Amorphous $Fe_{100-x}Tb_x$ alloy films in a composition range of 15 at.% $\leq x \leq$ 29 at.% possess PMA indicated with region II to IV in Fig. 2.5a, while the reversal mechanism changes slightly in the different regions due to the varying net saturation magnetization. Beside the observed out-of-plane easy axis the total value of the anisotropy constant is controversially discussed. Especially in the vicinity of the compensation point the exact behavior is unknown. Minimum as well as maximum values for PMA at the compensation point are reported by several groups as outlined in Fig. 2.6a, b, respectively [24, 25]. This uncertainty is attributed to the manifold peculiar structural properties present in the amorphous alloy related to the different preparation techniques, film thicknesses, and seed layers, which determine the intrinsic magnetic properties like the distribution of the local anisotropy becoming very influential at the compensation point.

The alloy composition is not exclusively influencing the magnetic properties, film thickness plays also an important role. In Fig. 2.7 the coercivity and net saturation magnetization is shown as a function of the thickness of amorphous $Fe_{80}Tb_{20}$ films [13]. With thinner alloy films the saturation magnetization increases while the coercivity decreases, which is related the growth conditions within the first 10-nm-regime where the substantial influence of the substrate produces a strong magnetic in-plane component in the alloy. Thicker layers exhibit a dominant PMA imprinted by the

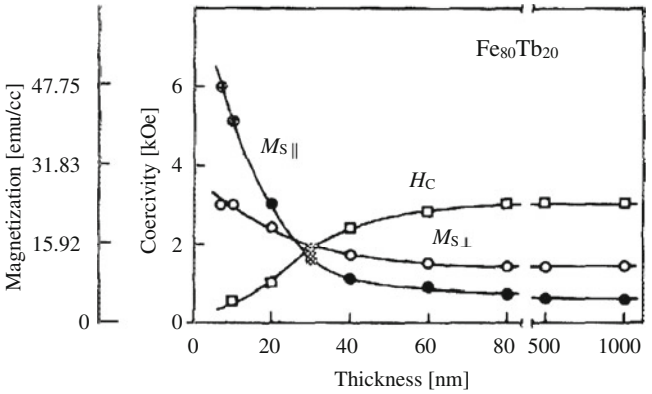

Fig. 2.7 Coercivity and saturation magnetization of $Fe_{80}Tb_{20}$ films at RT with varying thickness [13]. Two different saturation values for the magnetization are given for in-plane and out-of-plane field geometry

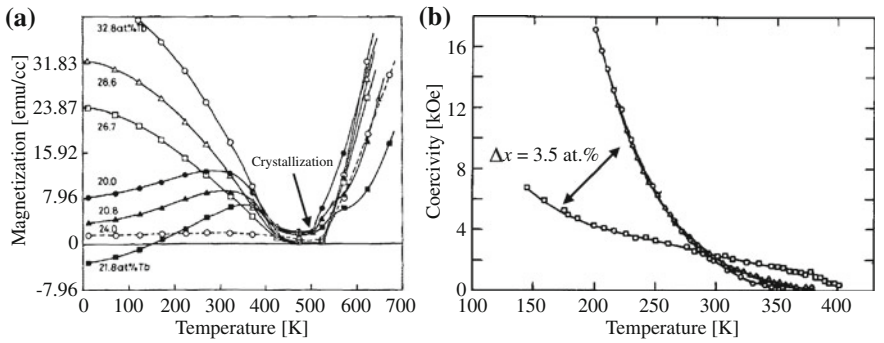

Fig. 2.8 **a** Temperature dependence of the resulting net magnetization of 1-μm-thick Fe–Tb films with different compositions [13]. **b** Coercivity of 100-nm-thick Tb rich Fe–Tb films as a function of temperature [26]. A variation in Tb content of only 3.5 at.% leads to strong differences in the temperature dependency

anisotropy in the chemical short range order due to the directed growth process as mentioned in the previous section.

Furthermore, the sperimagnetic Fe–Tb alloy films show a strong temperature dependence in the net saturation magnetization and coercivity due to the orientational distribution of the Tb moments (see Fig. 2.4b) [13, 26]. In general a strong increase of the Tb sublattice moment towards lower temperatures causing a relative decrease in the net magnetization dominated by the Fe sublattice is observed as outlined in Fig. 2.8a. Depending on the Tb concentration different curve shapes are possible leading to the existence of a compensation point and dominant Tb sublattice magnetization in the lower temperature regime. Figure 2.8b presents the temperature dependence of the coercivity of 100-nm-thick Tb dominated Fe–Tb films.

The increase with decreasing temperature originates from the strong enhancement of magnetic anisotropy, which also strongly depends on the alloy stoichiometry.

Following the known properties of the amorphous Fe–Tb alloy system with regard to the frame of this work $Fe_{100-x}Tb_x$ films with thicknesses between 5 nm and 50 nm in a composition range from 14 to 30 at.% Tb were produced using magnetron co-sputtering technique.

2.4 Magnetostriction

The magnetostriction as intrinsic behavior of magnetic materials describes the influence of the magnetization onto the structural properties and *vice versa*. Generally, the structure interacts via crystal field and spin-orbit coupling with the magnetization. Thus, changes in the direction of the intrinsic magnetic moments may produce changes in the inter atomic distances inducing stress and deformations in the material. The volume or length change between the saturated and demagnetized state is denoted as saturation magnetostriction constant λ_S and can be deduced from the size difference normalized to the initial size in demagnetized state $\lambda_S = \frac{\Delta V}{V}$.

The highest value of magnetostriction, of the order of 2.5×10^{-3} was found in the crystalline Laves phase of $TbFe_2$ by A. E. Clark and H. S. Belson in 1972 [27]. Compared to elemental Co with a magnetostriction constant of about 0.06×10^{-3} this Laves phases possess a very strong influence of the magnetic field on the structure. However, this alloys exhibit also strong magnetocrystalline anisotropy making them unsuited for magnetoelastic applications due to the high saturation fields they require. Therefore, extensive research was done concerning amorphous rare-earth-transition-metal alloys [9]. Since the magnetostrictive effects in this amorphous materials are related to magnetoelastic interactions between local strains and anisotropies controlling the direction of magnetic moment, relatively high magnetostriction constants with moderate magnetic anisotropies are possible already at RT [4]. Particularly, amorphous Fe–Tb alloy films exhibit magnetostriction constants between 0.1×10^{-4} and 1×10^{-4} varying with the Tb concentration as outlined in Fig. 2.9 [23]. The high magnetostrictive values take place above 30 at.%, which goes along with the strain induced transition of the easy axis from out-of-plane to in-plane direction. This adjustability of anisotropy and magnetostriction with the Tb content makes this system suitable for application.

Concerning the purpose of this work magnetostriction plays a minor role, since all films were prepared with thicknesses less than 50 nm on thick non-elastic substrates keeping the magnetostrictive influence rather small. Furthermore, the used $Fe_{100-x}Tb_x$ alloy films in a composition range from 14 to 30 at.% Tb reveal changes in the magnetostriction constant less than half an order of magnitude (see Fig. 2.9).

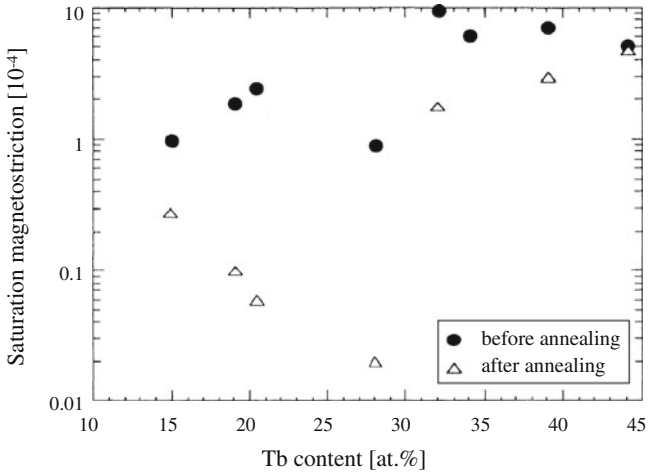

Fig. 2.9 Saturation value of the magnetostriction coefficient of amorphous $Fe_{100-x}Tb_x$ alloy films depending on the Tb content for as grown and annealed films [23]

2.5 Fe–Tb Films for Application

In the past thin amorphous Fe–Tb alloy films were used in magneto-optical data storage devices due to its high magnetic anisotropy and the ability to form stable bubble domains [28–30]. The relatively low Curie temperature at around 400 K of the alloy system provide the ability for technical suitable Curie point writing where a short laser pulse heats the magnetic film locally to T_C giving rise to bubble domain formation induced by the stray field and the guided external applied magnetic field when the temperature becomes reduced below T_C again [11, 30]. As one data bit is represented by one bubble domain the storage density is limited to the stability condition and minimum radius of the bubble with respect to the material [31, 32]. Additionally, the optical resolution of the laser spot is limited by its wave length. Both limitations restrict the achievable maximum areal density. For this reason magneto-optical data storage was overtaken by magnetic data storage in granular media using conventional inductive write heads as superior in performance. Due to this magnetic data storage is now the common storage technic available on the market.

Since nowadays the areal density in CoCrPt based perpendicular granular media approaches more and more to its maximum limit (1 Tbit/inch^2) due to the super-paramagnetic effect [33–35], new storage concepts come up providing new routes to achieve ultra high storage densities beyond 1 Tbit/inch^2. One of these concepts is heat assisted magnetic recording (HAMR) where a localized laser heat pulse provides writability (near the Curie temperature) for high anisotropic magnetic materials like ordered $L1_0$ FePt [36] used in order to guarantee magnetization stability in grains with sizes below 5 nm [37, 38].

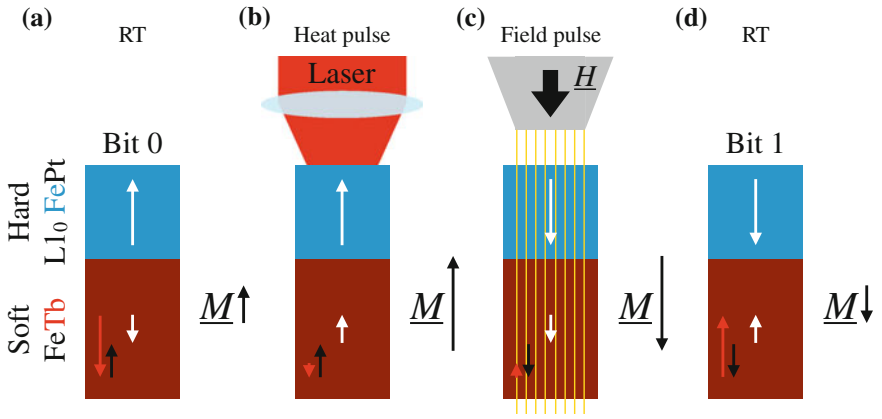

Fig. 2.10 Schematic drawing of the heat assisted reversal process in ECC media with soft Fe–Tb as functional layer. **a** The Fe–Tb layer is dominated by the Tb sublattice moment at RT. **b** The laser pulse heats the Fe–Tb layer above the compensation temperature and the net magnetization becomes dominated by the Fe sublattice leading to a parallel alignment to the hard $L1_0$ FePt layer. **c** The ECC layer stack with enhanced saturation magnetization becomes reversed by a magnetic field pulse via domain nucleation in the soft Fe–Tb layer. **d** After cooling down to RT the reversed magnetization state in the FePt layer becomes stabilized by the Tb dominated antiparallel oriented Fe–Tb layer. After this cycle the data bit is changed from zero to one

With regard to HAMR the temperature dependence of the magnetization is a key property needed to be controlled and adjusted to the purposes of the storage application. Thus, amorphous Fe–Tb alloy films represent a promising candidate for the use as a functional layer for HAMR media as the magnetization can be controlled easily by the Tb concentration and ambient temperature (see Sect. 2.3). In doing so, Fe–Tb alloy films can be utilized as soft magnetic layer in connection to a hard magnetic storage layer like $L1_0$ FePt forming an exchange coupled composite (ECC) media. This ECC media as suggested by Suess et al. [39, 40] provides high temperature stability due to the anisotropy of the hard magnet and overcomes the writability issue by nucleation of a domain wall in the soft magnet during the reversal as a sufficiently high switching field is applied. Concerning the Fe–Tb layer its FI structure stabilizes the magnetic configuration further by interfacial exchange coupling. In particular the temperature dependence of the magnetization can be adjusted so that the compensation point lies above RT. On one hand, this allows an antiparallel alignment between the Tb dominated Fe–Tb layer and the hard magnet at RT lowering the contribution of the stray field, which provides the mentioned bit stabilization. And on the other hand, at the high temperature state after heat pulse the net moment of the Fe–Tb layer becomes Fe dominant and aligns parallel to the moment of the hard magnet providing high saturation magnetization for the switching of the ECC layer stack. A schematic drawing for the heat assisted reversal of the proposed ECC media with functional Fe–Tb soft magnetic layer is presented in Fig. 2.10a–d. Please note, the readback of such ECC media is still an issue and requires innovative read concepts.

Beside the concept about the use of amorphous Fe–Tb alloy films in ultra high density HAMR media further applications are imaginable. Based on the magnetostriction present in the amorphous Fe–Tb alloy system as discussed in the previous chapter one can consider this material for micro force or vibration sensors following the approach of microelectromechanical systems (MEMS) with magnetic readout. Also a very strong interfacial exchange coupling in novel FI/F exchange-bias heterostructures is expected for this class of material due to non-existing grain boundaries, atomic steps, or dislocations at the interface making amorphous Fe–Tb alloy films feasible for magnetic field sensor and spin valve applications based on the giant and tunnel magneto resistance effect. A detailed discussion on this topic will be given within the chapter about the exchange-bias effect in FI/F rare-earth-transition-metal based heterostructures.

References

1. H. König, Naturwissenschaften **33**, 71 (1946)
2. S. Kobe, A.R. Ferchmin, J. Mater. Sci. **12**, 1713 (1977)
3. K. Handrich, S. Kobe, *Amorphe Ferro- und Ferrimagnetika* (Akademie, Berlin, 1980), ISBN 978-3-87664-044-0
4. K.H. Buschow, *Handbook of Magnetic Materials*, vol. 6 (Elsevier, Amsterdam, 1991), ISBN 978-0-444-88952-2
5. J.A. Fernandez-Baca, *The magnetism of amorphous metals and alloys* (World Scientific, Singapore, 1995), ISBN 978-9-810-21033-5
6. T.B. Massalski, H. Okamoto, P.R. Subramanian, L. Kacprzak, *Binary Alloy Phase Diagrams* (ASM International, Materials Park, 1990). ISBN 978-0-87170-403-0
7. M.P. Dariel, J.T. Holthuis, M.R. Pickus, J. Common Met. **45**, 91 (1976)
8. I.G. Orlova, A.A. Eliseev, G.E. Chuprikov, E. Rukk, Zhurnal Neorganicheskoi Khimii **22**, 2557 (1977)
9. E. Wohlfarth, *Handbook of Magnetic Materials*, vol 1 (North-Holland Publishing Company, Amsterdam, 1980), ISBN 978-0-444-85311-0
10. J. Rhyne, J. Schelleng, N. Koon, Phys. Rev. B **10**, 4672 (1974)
11. Y. Mimura, N. Imamura, T. Kobayashi, IEEE Trans. Magn. **12**, 779 (1976)
12. Y. Mimura, N. Imamura, Appl. Phys. Lett. **28**, 746 (1976)
13. N. Sato, J. Appl. Phys. **59**, 2514 (1986)
14. J. Coey, J. Chappert, J. Rebouillat, T. Wang, Phys. Rev. Lett. **36**, 1061 (1976)
15. J. Coey, J. Appl. Phys. **49**, 1646 (1978)
16. J. Rebouillat, A. Lienard, J. Coey, R. Arrese-Boggiano, J. Chappert, Physica B **86**, 773 (1977)
17. J.J. Rhyne, *Handbook on the Physics and Chemistry of Rare Earths*, vol. 2 (North-Holland Publishing Company, Amsterdam, 1979), ISBN 978-0-444-85021-X
18. I. Campbell, J. Phys. F: Met. Phys. **2**, L47 (1972)
19. C. Robinson, M. Samant, Appl. Phys. A Mater. Sci. Process. (1989)
20. M. Tewes, J. Zweck, H. Hoffmann, J. Magn. Magn. Mater. **95**, 43 (1991)
21. V.G. HarriS, K.D. Aylesworth, B.N. Das, W.T. Elam, N.C. Koon, Phys. Rev. Lett. **69**, 1939 (1992)
22. T. Hufnagel, S. Brennan, P. Zschack, B. Clemens, Phys. Rev. B **53**, 12024 (1996)
23. J. Huang, C. Prados, J. Evetts, A. Hernando, Phys. Rev. B **51**, 297 (1995)
24. Y. Mimura, N. Imamura, T. Kobayash, A. Okada, Y. Kushiro, J. Appl. Phys. **49**, 1208 (1978)
25. R. Van Dover, M. Hong, E. Gyorgy, J. Dillon, S. Albiston, J. Appl. Phys. **57**, 3897 (1985)
26. R. Malmhäll, T. Chen, Thin Solid Films **125**, 257 (1985)

27. A. Clark, H. Belson, Phys. Rev. B **5**, 3642 (1972)
28. M. Kryder, Ann. Rev. Mater. Sci. **23**, 411 (1993)
29. Y. Aoki, IEEE Trans. Magn. **MAG-20**, 1022 (1984)
30. S. Tsunashima, J. Phys. D: Appl. Phys. **34**, R87 (2001)
31. J. Nielsen, Metall. Mater. Trans. B **2**, 625 (1971)
32. J. Nielsen, Ann. Rev. Mater. Sci. **9**, 87 (1979)
33. H.J. Richter, A. Lyberatos, U. Nowak, R.F.L. Evans, R.W. Chantrell, J. Appl. Phys. **111**, 033909 (2012)
34. R. Evans, R.W. Chantrell, U. Nowak, A. Lyberatos, H.J. Richter, Appl. Phys. Lett. **100**, 102402 (2012)
35. S. Piramanayagam, K. Srinivasan, J. Magn. Magn. Mater. **321**, 485 (2009)
36. S. Sun, C.B. Murray, D. Weller, L. Folks, Science **287**, 1989 (2000)
37. M. Kryder, E.C. Gage, T.W. McDaniel, W.A. Challener, R.E. Rottmayer, G. Ju, Y.T. Hsia, M.F. Erden, Proc. IEEE **96**, 1810 (2008)
38. F. Akagi, M. Mukoh, M. Mochizuki, J. Ushiyama, T. Matsumoto, H. Miyamoto, J. Magn. Magn. Mater. **324**, 309 (2012)
39. D. Suess, T. Schref, S. Fähler, M. Kirschner, Appl. Phys. Lett. **87**(1), 012504 (2005)
40. D. Suess, T. Schrefl, R. Dittrich, M. Kirschner, J. Magn. Magn. Mater. **290–291**, 551 (2005b)

http://www.springer.com/978-3-319-07105-3

Magnetic Order and Coupling Phenomena
A Study of Magnetic Structure and Magnetization Reversal Processes in Rare-Earth-Transition-Metal Based Alloys and Heterostructures
Schubert, C.
2014, XXI, 121 p. 74 illus., 18 illus. in color., Hardcover
ISBN: 978-3-319-07105-3